Integration of LiDAR and Landsat Data to Estimate Forest Canopy Cover in Coastal British Columbia

Oumer S. Ahmed[1*], Steven E. Franklin[2], and Michael A. Wulder[3]

Affiliations:

[1] Geomatics, Remote Sensing and Land Resources Laboratory, Department of Geography, Trent University, Ontario, K9J 7B8, Canada

[2] Department of Environmental and Resource Studies/Science, Department of Geography, and Office of the President, Trent University, Ontario, K9J 7B8, Canada

[3] Canadian Forest Service (Pacific Forestry Centre), Natural Resources Canada, 506 West Burnside Road, Victoria, British Columbia, V8Z 1M5, Canada

***** Corresponding author:

E-Mail address: osahmed@trentu.ca

Tel.: 705-748-1011 x 7965.

Pre-print of published version.

Reference:

Ahmed, O.S., S.E. Franklin, M.A. Wulder. (2014). Integration of LiDAR and Landsat Data to Estimate Forest Canopy Cover in Coastal British Columbia. Photogrammetric Engineering and Remote Sensing. Vol. 80, No. 10, pp. 953-961.

DOI: http://dx.doi.org/10.14358/PERS.80.10.953

Abstract
Airborne Light Detection and Ranging (LiDAR) data provide useful measurements of forest canopy structure but are often limited in spatial coverage. Satellite remote sensing data from Landsat can provide extensive spatial coverage of generalized forest information. A forest survey approach that integrates airborne LiDAR and satellite data would potentially capitalize upon these distinctive characteristics. In this study in coastal forests of British Columbia, the main objective was to determine the potential of Landsat imagery to accurately estimate forest canopy cover measured from small-footprint airborne LiDAR data in order to expand the LiDAR measurements to a larger area. Landsat-derived Tasseled Cap Angle (TCA) and spectral mixture analysis (SMA) endmember fractions (i.e. sunlit canopy, non-photosynthetic vegetation (NPV), shade and exposed soil) were compared to LiDAR-derived canopy cover estimates. Pixel-based analysis and object-based area-weighted error calculations were used to assess regression model performance. The best canopy cover estimate was obtained (in the object-based deciduous forest models) with a mean object size (MOS) of 2.5 hectares (adjusted R^2= 0.86 and RMSE = 0.28). Overall, lower canopy cover estimation accuracy was obtained for coniferous forests compared to deciduous forests in both the pixel and object-based approaches.

Key words: Canopy cover, Landsat, LiDAR, Spectral Mixture Analysis

1. Introduction

Accurate information on forest canopy structure is required to understand and manage forest ecosystems (Wulder and Franklin 2007). Forest canopy cover (CC), the area of the ground covered by a vertical projection of the canopy (Jennings et al., 1999), is a useful metric for several natural resource management applications such as: evaluation of wildlife habitat (Koy et al., 2005), forest structure classification (Lovell et al., 2003; Fiala et al., 2006; Lee and Lucas 2007), characterization of carbon sinks (Chopping et al., 2008), forest fire behaviour and fuel models (Rollins and Frame, 2006), and estimation of canopy light transmission (Lieffers et al., 1999).

Canopy cover is typically estimated with field instrumentation at specific sites, or by remote sensing methods at increasing spatial scales to support large area monitoring and modeling applications (e.g., Canadell et al., 2008, Coulston et al., 2012). Airborne LiDAR (Light Detection and Ranging) is an active remote sensing system well suited to measure canopy structural attributes. LiDAR data have proven useful for estimating CC (Hyde et al., 2005; Smith et al., 2009, Hall et al., 2011); while LiDAR data can provide better estimates

of CC, wall-to-wall acquisitions of LiDAR data remain cost prohibitive for large forest areas (Coulston et al., 2012). Therefore, LiDAR-based characterizations of canopy structure are often restricted in spatial extent. Multispectral remote sensing datasets such as the one from Landsat have also been employed to estimate CC. Yet, the lesser sensitivity of these spectral datasets to the three dimensional structure of vegetation canopies (Falkowski et al., 2005; Duncanson et al., 2010) often degrades the relationship between CC and metrics calculated from the spectral bands. However, the free availability of large area multispectral datasets makes them an important data source for estimating CC across large areal extents.

In one recent study, Smith et al. (2009) conducted cross-comparison of multispectral, LiDAR and coincident field measurements of CC data and they found the relationship between LiDAR-derived and field-measured canopy cover was much stronger and more linear. As forest information is considered over larger areas, and at higher temporal resolution (e.g., Goetz et al., 2009), such airborne LiDAR data must be supplemented with other remote sensing datasets, such as those acquired by the sensors on the Landsat series of platforms (Wulder et al., 2003). The integration of LiDAR and passive optical sensors needs to be more thoroughly explored for wall-to-wall mapping of canopy cover (Hall et al., 2011). Recently, models have been developed to spatially extend airborne LiDAR measured forest structural attributes over larger areas using parametric approaches (Chen et al., 2012), which typically use pixel-based multiple regression to define relationships between the satellite imagery and airborne LiDAR-derived canopy cover (e.g., Smith et al., 2009). The integration of such satellite multispectral remote sensing data with information from airborne LiDAR provides opportunities to capitalize upon the distinctive characteristics of both. This integration could also serve to make LiDAR more cost effective over larger areas (e.g., Hudak et al. 2002; Chen et al. 2012). While dealing with methods to accomplish airborne LiDAR and Landsat data integration, among the significant questions that must be addressed are: (i) the selection of Landsat spectral variables and (ii) the selection of a pixel-based or object-based sampling approach.

Recent studies have developed empirical models to produce canopy cover products (e.g., Coulston et al., 2013) using explanatory variables derived from Landsat reflectance values and derivatives. Various Landsat indices have also been used to estimate forest structure

characteristics. The Tasseled Cap (Kauth-Thomas) Transformation indices, for example, have proven reliable and robust in a range of environments (Healey et al., 2005). To accommodate the lack of short-wave infrared bands when assembling a time series of Landsat images including both Multispectral Scanner (MSS), Thematic Mapper (TM), and Enhanced Thematic Mapper (ETM+), the Tasseled Cap Angle (TCA) is recommended (Powell et al. 2010). Generally, the TCA is an estimate of the proportion of vegetation to non vegetation (Powell et al., 2010; Gomez et al., 2011). Dense forest stands are expected to show higher TCA values than more open stands or bare soil (White et al., 2011). The use of fraction images derived from Spectral Mixture Analysis (SMA) has also shown to be effective in estimating forest canopy cover (Goodwin et al., 2005; Elmore et al., 2000; Lobell et al., 2002; Peddle et al., 1999). When selecting a pixel-based or object-based approach for image analysis, different methodological challenges are posed (Hay and Blaschke 2010). For example, in an object-based approach, a significant question is the best object scale (i.e., mean object size (MOS)) to achieve the desired model accuracy. There is a growing literature of research reporting the differences in estimation accuracy between pixel-based and object-based models over a range of scales (e.g., Clinton et al., 2010; Duro et al., 2012; Duro et al., 2013).

The objective of the current study is to examine the choice of Landsat spectral variables and the pixel-based versus object-based approach in determining the relationship between airborne LiDAR-derived forest canopy cover and Landsat imagery acquired over deciduous and coniferous forests in Vancouver Island, British Columbia.

2. Data and Methods

2.1 Study area

The study area (49°52′N, 125°20′W) is located between Courtenay and Campbell River on eastern Vancouver Island, British Columbia, Canada (Figure 1). A 5.1 by 5.1 km (2601 ha) study area corresponding to the airborne LiDAR data acquisition mission ranges in elevation from 120m to 460m, and is within 15 km of the coast. The area is characterized by mature conifer forest, regenerating conifer and deciduous stands, and harvested areas. Conifer forest types comprise approximately 65% of the study area, and are dominated by 80% Douglas-fir [Pseudotsuga menziesii (Mirb.) Franco], with smaller proportions of Western Red Cedar [Thuja plicata (Donn.)], and Western Hemlock [Tsuga heterophylla

(Raf.) Sarg.]. Deciduous forest of Red Alder (Alnus rubra Bong.) comprises approximately 16% of the study area. The majority of forest stands within the area, which are industrially managed by private forest companies under license from the provincial government, consists predominantly of forest regenerating from harvest and are between 20 and 60 years of age (Morgenstern et al., 2004), with a mean canopy height of 18.5 m. For the mature stands, a 1998 site survey found that the stand density was approximately 1100 stems/ha.

2.2 Airborne LiDAR data

Discrete return LiDAR data for the study area were acquired on 8 June 2004 by Terra Remote Sensing (Sidney, British Colombia, Canada) using a Lightwave Model 110 Terrain Scanning LiDAR from a Bell 206 Jet Ranger helicopter. The positioning systems, a Litton LTN-92 inertial navigation system (INS) and an Ashtech Z-surveyor Dual Frequency P-code differential global positioning system (DGPS), recorded the aircraft's altitude and position within 5–10 cm. The Lightwave Model 110 has a pulse repetition frequency of 10 kHz, a wavelength of 1047 nm, a swath width of 56°, and a beam divergence of 3.5 mrad. Based on the pulse frequency, lowest sustainable flight speed, and altitude, hit densities of 0.7 hits/m^2 were achieved with a footprint (spot size) of 0.19m (Table 1).

No artificial objects (e.g., buildings) exist in the study area. The raw LiDAR point cloud data were collected containing both ground and non-ground returns and were processed with Terrascan software (v4.006 – Terrasolid, Helsinki, Finland) which combines filtering and thresholding methods (Chen et al., 2010). In this study, LiDAR-derived canopy cover (CC), was estimated using the ratio of the pulse returned from the upper layer of tree crown (determined using a threshold height) to total returns (throughout the canopy to ground profile).

$$CC = \frac{\sum \text{all returns (above some height threshold)}}{\text{total returns}} \quad (1)$$

This CC derivation method has been demonstrated in several previous studies, including: Hyde et al., (2005), Morsdorf et al., (2006), Solberg et al., (2006), Hopkinson and Chasmer, (2009), and Smith et al. (2009). Common to these examples in the literature, the selection of the threshold above which returns are considered to be from canopy has been determined based upon local forest conditions, the goals of the study, and the desired information. To better understand the implications of differing threshold values Smith et al. (2009) evaluated a selection of different height thresholds over a study area with mixed forest conditions. Their analysis determined a negligible variation in correlation (r difference of ~0.0005) between the field-densitometer-derived and LiDAR derived canopy cover measures occurred when the threshold was between 1.00 and 2.00 m; therefore, for their

study they selected an intermediate threshold of 1.50 m. The same threshold value of 1.50 m was used in our study to determine canopy returns. The final estimates of canopy cover and other structure variables were resampled to 30m to match the spatial resolution of the Landsat imagery

2.3 Landsat data

A Landsat image of the study area acquired August 16, 2004 was obtained from the United States Geological Survey (USGS) Landsat archive. The image was system-corrected for terrain and converted to 'top-of-atmosphere-radiance' (L1T data product). The cosine estimation of atmospheric transmittance (COST) absolute radiometric correction model of Chavez (1996) was applied to convert to surface reflectance. Water, clouds and cloud shadows in the image were masked using an object-based cloud and cloud shadow detection algorithm for Landsat imagery (Zhu et al., 2011). Finally, the airborne LiDAR data were registered to the Landsat image using 50 ground control points. A second-order polynomial warping method and nearest neighbor resampling were selected for the co-registration, yielding a RMSE of 0.59 m.

The Landsat image was transformed using the Tasseled Cap (Kauth-Thomas) Transformation with coefficients specific to the image date and sensor (Crist, 1985; Huang et al., 2002). The Tasseled Cap Angle (TCA), defined by Powell et al. (2010) was derived for the Landsat image in this study (see Ahmed et al., 2014). TCA has been interpreted as an indicator of the proportion of vegetation to non-vegetation within a Landsat pixel, and is defined as follows:

$$TCA = \arctan(\text{greenness} / \text{brightness}) \quad (2)$$

Spectral mixture analysis (SMA) is a useful technique used to address the spectral heterogeneity present in remote sensing pixels (e.g., Peddle et al., 1999; Zeng et al., 2008). SMA estimates the proportions of pure components within each pixel, which typically contains more than one feature or ground cover type (Somers et al., 2011). In this study, spectral mixture analysis (SMA) was used to estimate the proportions of pure components (i.e., endmembers) within Landsat pixels. Using the 2004 Landsat TM imagery we generated sub-pixel fraction images. Lu et al. (2004) demonstrated that the removal of highly correlated bands such as TM 1 and TM 2 in SMA improves the quality of fraction images. Thus, in this study to reduce correlation and data redundancy we used Landsat TM band subset images (i.e. bands 3, 4, 5, and 7) in the SMA. One of the important prerequisite for successful SMA is the selection of representative endmembers (Somers et al., 2011; Tompkins et al., 1997). Here endmembers representing Sunlit canopy, non photosynthetic vegetation (NPV), exposed soil, and shade were derived from the Landsat multispectral image using the n-dimensional visualization tool (available in ENVI 4.8) and the LiDAR data. Typically, the variation in understory reflectance across 30 m resolution Landsat

scene causes a difficulty in SMA endmember selection, in this study to reduce the influence of understory vegetation on SMA fractions, tree height information derived from LiDAR was used to help in the selection of endmembers. For example, tree height information derived from LiDAR aided in the selection of NPV and exposed soil endmembers by identifying sites with low or no vegetation cover. The pixels positioned at the edges of the data cloud of the Landsat spectral space in the n-dimensional visualization tool were selected as sample endmembers. Finally, the endmembers were selected based on the spectral shape of the wavelenghth-reflectance and image information (e.g. the spectra for soil are mostly associated with dirt roads and NPV is mostly associated with understory grass having senesced vegetation). We applied least-square linear mixture modeling (Adams et al., 1993) to estimate the proportion of each endmember within the Landsat pixels. The sums of the fractions add up to 1. The n-dimensional visualisation tool was also used to check the separability of the endmembers and refine the selected regions of interest. The SMA model results were evaluated as proposed by (Adams et al. 1995) with the root-mean-square (RMS) image and fraction images interpreted in terms of image context and spatial distribution. Finally the fractional abundances of the key image endmembers (sunlit crown, NPV, bare soil, and shade) were estimated.

2.4 Sample Selection

The use of segmentation objects, from Landsat spectral data, as areal units to estimate airborne LiDAR-derived canopy cover was compared with the results of estimates obtained using areal units of fixed 30 m size (Landsat pixels). Systematic sampling was used to select data from the Landsat and LiDAR imagery for the regression analysis. Tree height information from the LiDAR Crown Height Model (CHM) described by (Chen et al., 2010) was used to aid in distinguishing various ground features, such as trees from non-treed low vegetation. Various other sources of data aided in producing the stratification, including an existing land cover classification (Wulder et al., 2008) and the provincial database "Terrestrial Ecosystem Mapping of Site Series" (2005) for the study area. These sources were also used to identify the dominant forest types in the area.

In the pixel-based sample, a sampling procedure was designed based on semivariograms of the airborne LiDAR-derived canopy cover. Typically, the semivariance stabilized at 250–300 m suggesting that spatial autocorrelation was significant within a lag of 300m. A minimum 10 Landsat pixel buffer was then enforced between sampled pixels. The starting pixel was randomly selected from a subsample of 100 pixels near the northwest border of the LiDAR dataset. From the random starting pixel, every tenth pixel was sampled when possible. Following this procedure two independent samples were obtained for statistical model-building and validation of the model.

In the object-based sample, objects of varying size and shape resulted from applying a multiresolution segmentation using the ENVI 4.8 feature extraction module on the Landsat

TCA image. Ten different object scales or minimum object size (MOS) were examined. Due to the variation in data acquisition geometry between the LiDAR and the Landsat sensor the model performance using a MOS smaller than 0.074 ha was highly affected by the co-registration errors mainly in areas where large canopy cover variation exists, thus a MOS of 0.074 hectare was selected as the smallest scale in this study. The MOS of 7.00 ha was chosen as the largest scale, when using a MOS greater than 7.00 ha the output segments start to contain various land cover types instead of a single cover type within a given object. Finally, the patchiness of the study area due to the resulting segments was examined using percent homogenous cover calculated for variable minimum object sizes (MOS).

The same spectral variables were extracted for the object-based analysis. However, all variables were extracted from objects rather than pixels. Model building and validation samples were selected similar to the pixel-based approach. Here buffered random sampling was used, in which image objects were randomly selected but prevented from being closer together than the ideal limit of 300m where the spatial autocorrelation was found to be significant. Subsequently 40 samples were selected for each model building and validation. The final model RMSE was calculated in a slightly different way when using the object-samples. Unlike the pixel-based approach, in the object based approach image objects have varying sizes even at the same scale. This causes large objects to have more influence in the canopy cover error calculation than small objects. Thus, for the model validation it is important to consider each object based on the size of its area. In this study we applied an area weighted RMSE used by Chen et al. (2011).

$$RMSE = \sqrt{\frac{1}{A_n}\sum_{i=1}^{N}[Ai(CC_{Landsat\_i} - CC_{LiDAR\_i})^2]} \qquad (3)$$

Where $CC_{Landsat\_i}$ = Canopy cover calculated from the regression using Landsat imagery for the i^{th} object; CC_{Lidar_i} = Canopy cover measured from LiDAR data for the ith object; A_i = area for the i^{th} object; A_N = area for the total study area; N = total number of objects.

A check of the multicollinearity between predictor variables in the regression analysis was carried out among the Landsat spectral indices. Ordinary least squares (OLS) regression models were developed to estimate LiDAR-derived canopy cover with the predicting variables derived from Landsat spectral indices (TCA) and fractional abundances of the key image endmembers (sunlit crown, NPV, bare soil, and shade). The statistical analysis was designed to assess the relationship between the LiDAR-derived canopy cover estimates and the Landsat TCA, and to evaluate the contribution of spectral mixture analysis endmember fractions, sunlit canopy, non-photosynthetic vegetation (NPV), shade and soil information derived from Landsat imagery to the accuracy of canopy cover estimation. This was achieved by building an exhaustive list of models, using all possible combinations of available predictors, in a forward stepwise method. All residuals were used to calculate

RMSE for each validated model. Consequently, the R^2 and RMSE were selected to evaluate model performance.

3. Results and discussion

The spectral reflectance of the four SMA extracted endmembers (sunlit crown, NPV, bare soil, and shade) as derived from Landsat shortwave-infrared, near-infrared and red bands are presented in Fig. 2. The endmembers were extracted following the methods indicated in Section 2.3 and were used to estimate the airborne LiDAR-derived canopy cover.

The airborne LiDAR-derived canopy cover estimate, Landsat-derived TCA and endmember fractions (i.e. sunlit crown, NPV, exposed soil, and shade) for the study area are shown in Fig. 3. Spatial patterns are visible that coincide with an interpretation of the disturbance history of the study area; for example, in the upper left hand corner of the study area are patches that appear dark in the LiDAR-derived canopy cover image, and bright in the exposed soil endmember fraction image. Such areas are recently harvested forests that are in the early stage of regeneration, with low canopy cover and high degree of not yet fully revegetated. Similarly, in the lower left hand portion of the study area, in the LiDAR-derived forest canopy cover estimate patterns are visible that show previously harvested forest stands in various stages of regeneration. These areas are much brighter in the LiDAR-derived forest canopy image and darker in the TCA and various endmember fraction images. This qualitative interpretation of visible patterns in the LiDAR and Landsat imagery suggests that a quantitative regression analysis can be used to document the relationship in more detail.

In the pixel-based sample, the individual correlation coefficients between TCA, SMA-derived endmember fractions and the airborne LiDAR-derived canopy cover estimate are shown in Table 2. As expected, a strong correlation coefficient was obtained for the TCA ($r = 0.86$; $R^2 = 0.73$). A lower correlation was observed between LiDAR-derived canopy cover and the sunlit canopy endmember fraction ($r = 0.68$; $R^2 = 0.46$), and the lowest correlation coefficient was obtained using the exposed soil endmember.

Most of the possible combinations of the Landsat TCA and the spectral endmembers produced significant multiple regression models with LiDAR-derived canopy cover (Table 3). Adjusted R^2 values ranged from 0.15 to 0.81. In this study only those models with adjusted R^2 of ≥ 0.65 were considered, which resulted in seven regression models selected for coniferous and deciduous forests (Table 3 and 4). For all combinations each independent variable was evaluated and retained if its correlation value with any other independent variable was lower than 0.7.

The coniferous forest regression models predicting LiDAR-derived canopy cover suggest the accuracy limit for the application of Landsat in large-scale studies of canopy cover. The best predictor model was obtained using the combination of TCA, sunlit canopy and the soil endmember, resulting in multiple $R = 0.88$, $R^2 = 0.78$ and an adjusted $R^2 = 0.78$.

Comparably this method gives better canopy cover estimation than previous studies which used Landsat shortwave infrared derived indices. For example, Ahmad et al. (2014) reported an adjusted R^2 = 0.76 when combining TCA and NDVI in similar regression models.

A lower estimation accuracy was obtained for conifer stands (R^2= 0.74) when TCA was used alone. The inclusion of endmember image fractions resulted in an overall better canopy cover estimation for conifers (R^2 = 0.78 and RMSE = 0.39) (Table 3). The pixel-based deciduous forest models indicate a better canopy cover estimation for deciduous forests (R^2= 0.81 and RMSE = 0.34) than for coniferous forests (Table 4).

The multi scale segmentation resulted objects of varying size and shape. The percent homogenous cover (Table 5) indicates the degrees of patchiness of the study area for six minimum object sizes (MOS). As MOS increased the subtle levels of patchiness declined. Small patches either aggregated into larger patches or completely disappeared leading to an increase in percent homogenous cover. Large MOS are expected to decrease the canopy cover variability between objects and increase the canopy cover variability within individual objects, whereas small MOS tend to decrease canopy cover variability within each object and the canopy cover variability between objects is expected to increase.

The performance of object-based coniferous models at 3 scales with MOS 2.0, 2.5 and 3.0 ha, which resulted in $R^2 \geq 0.60$ are shown in table 6. The object-based approach results for coniferous forest indicate the best object size for our study site corresponds to MOS of 2.5 hectares with adjusted R^2 = 0.82. This object-based approach resulted in better canopy cover estimation as compared to the pixel-based coniferous forest regression models. The error trend of regression models indicated that the regression models developed above MOS 3.0 and bellow MOS 2.0 have higher RMSE and lower R^2. Similar to the pixel-based approach the inclusion of endmember fractions, here also, resulted in a better estimation.

The object scale appears to play a more significant role for the deciduous forest sample than for the conifer stands. In this study, the best prediction of the LiDAR-derived canopy cover estimate was obtained using the spectral variables in the object-based deciduous models with MOS of 2.5 hectares resulting in adjusted R^2= 0.86 and RMSE = 0.28 (Table 7). A recent study by Chen et al. (2011) found that the best object scale corresponds to MOS of 4.00 ha for prediction of LiDAR-derived canopy height in the same study site. Since canopy cover is more closely associated with the two-dimensional satellite data than canopy height, in our study, a smaller MOS and improved estimation accuracy were obtained for LiDAR-derived canopy cover compared to the canopy height study by Chen et al. (2011). The best MOS of 2.5 ha found in our study is closer to the 2.0 ha minimum mapping unit used for inventory purposes by provincial and territorial forest management agencies in Canada. Hence, we are gaining confidence in the capacity for approaches such as that presented here to be used to generate unique values in areas not subject to regular forest inventory and to aid with update within inventory cycles over managed forests.

4. Conclusion

In this study, we investigated the potential of Landsat imagery to estimate forest canopy cover measured from small-footprint airborne LiDAR data in order to expand the LiDAR measurements to a larger area. Landsat-derived Tasseled Cap Angle (TCA) and spectral mixture analysis (SMA) endmember fractions (i.e. sunlit canopy, non-photosynthetic vegetation (NPV), shade and exposed soil) were compared to LiDAR-derived canopy cover estimates. Our results show that the inclusion of the endmember fractions considerably increased the model performance versus only using TCA. Conifer and deciduous forests were separately modelled using OLS regression, to better describe the impact of distinctive crowns and leaf shapes that produce fairly explicit spectral signatures in the study area. Pixel and object-based models were developed. An area-weighted error calculation approach was used to evaluate the RMSE of canopy cover derived from the object-based approach. In both pixel and object-based approaches the deciduous forest regression models predicting LiDAR-derived canopy cover resulted higher correspondence than coniferous models. Specifically, the average errors decreased by 82.4 percent (from 0.34 to 0.28) for deciduous forests. The results indicate that the best object models achieved better results than those developed using only the pixel-based approach. The best canopy cover estimate was obtained (in the object-based deciduous forest models) with a mean object size (MOS) of 2.5 hectares (adjusted R^2= 0.86 and RMSE = 0.28). We confirm that selecting suitable object scale plays a significant role in the object-based approach (Addink et al. 2007, Chen et al. 2011); since random scale selection may result in lower coefficient of determination than the pixel-based approach. This study demonstrates that changes in object scale affect the overall patchiness of the study area and the resulting canopy cover estimation. Generally the study area was found to have a less patchy landscape, the percentage homogeneous cover varying from 82% - 88% for the six minimum object sizes (MOS) that are considered in this study. Accordingly, when object scale was altered, subtle changes in the level of patchiness were found. The percentage homogonous cover for the study area at the optimum mean object size (MOS) of 2.5 hectares was 86.6%. When estimating continuous forest biophysical properties such as canopy cover, typical object based modeling approaches tend to focus only on the performance of regression models, regardless of object size. In this paper, we evaluated both the performance of regression models and the impact of changing object scale on the estimation of canopy cover. The optimum mean object size found in this study can be generalized for other areas with a similar degree of patchiness as the one considered in this study. For more heterogeneous areas with distinct patchiness and landscape characteristics the methodology used in this study can be applied to determine the optimum object size that can be applicable to the specific landscape conditions present. Additional focused research is suggested to assess the effect of object scales on attribute performance, aimed at providing insights that will allow for tuning of parameters to fit what is known about a given study location. The

parameters we used in this study offer an example or a basis for applications in other environments, with an investigation of applicability to be tested, as we suggest, and tuning when and if required.

Acknowledgements

The authors are grateful to the referees and the journal Editor for their constructive comments that helped improve the paper. This study was funded by the Natural Sciences and Engineering Research Council and the Canadian Forest Service, Natural Resources Canada. The authors also acknowledge the valuable discussions with Joanne C. White at the Canadian Forest Service, Natural Resources Canada.

References

Adams, J. B., D. E. Sabol, V. Kapos, R. F. Almeida, D. Robert, M. O. Smith, and A. R. Gillespie, 1995. Classification of multispectral images based on fractions of endmembers: Application to land-cover change in the Brazilian Amazon, *Remote Sensing of Environment*, 52:137–154.

Adams, J. B., M. O. Smith, A. R. Gillespie, 1993. Imaging spectro-scopy: Interpretation based on spectral mixture analysis, *Remote Geochemical Analysis: Elemental and Mineralogical Composition*, (V. M. Pieters and P. Englert, editors), New York: Cambridge Univ. Press, 7 pp. 145–166.

Addink, E.A., S.M. de Jong, and E.J. Pebesma, 2007. The importance of scale in object-based mapping of vegetation parameters with hyperspectral imagery, *Photogrammetric Engineering and Remote Sensing*, 73:905–912.

Ahmed, O.S., S. E. Franklin, M. A. Wulder, 2013. The interpretation of forest disturbance using Landsat imagery time-series and airborne LiDAR-derived canopy cover data in British Columbia, *Canadian Journal of Remote Sensing*, 39(6):521-542. doi: 10.5589/m14-004.

Canadell, J.G., and M.R. Raupach, 2008. Managing forests for climate change mitigation, *Science* 320:1456-1457.

Chavez, P., 1996, Image-based atmospheric corrections revisited and improved, *Photogrammetric Engineering and Remote Sensing*, 62:1025–1036.

Chen, G., and G.J. Hay, 2011. A support vector regression approach to estimate forest biophysical parameters at the object level using airborne lidar transects and Quickbird data, *Photogrammetric Engineering and Remote Sensing*, 77(7):733–741.

Chen, G., G.J. Hay, G. Castilla, B. St-Onge, and R. Powers, 2010. A multiscale geographic object-based image analysis to estimate lidar measured forest canopy height using Quickbird imagery, *International Journal of Geographical Information Science*, 25(6):877–893.

Chen, G., G.J. Hay, and B. St-Onge, 2012. A GEOBIA framework to estimate forest parameters from lidar transects, Quickbird imagery and machine learning: A case study in Quebec, Canada, *International Journal of Applied Earth Observations and Geoinformation*, 15:28−37.

Chopping, M., G.G. Moisen, L.Su, A. Lalibrete, A. Rango, J. Martonchik, and D.P.C. Peter, 2008. Large area mapping of southwestern forest crown cover, canopy height, and biomass using the NASA Multiangle Imaging Spectro-Radiometer. *Remote Sensing of Environment*, 112:2051–2063.

Coulston, J.W., D.M. Jacobs, C.R. King, and I.C. Elmore, 2013. The influence of multi-season imagery on models of canopy cover: A case study, *Photogrammetric Engineering and Remote Sensing*, 79(5):469–477.

Coulston, J. W., G. G. Moisen, B. T. Wilson, M. V. Finco, W. B. Cohen, and K. C. Brewer, 2012. Modeling percent tree canopy cover: A pilot study, *Photogrammetric Engineering and Remote Sensing*, 78(7):715–727.

Crist, E. P., 1985. A TM tasseled cap equivalent transformation for reflectance factor data, *Remote Sensing of Environment*, 17:301–306.

Duncanson, L., K.O. Niemann, and M.A. Wulder, 2010. Integration of GLAS and Landsat TM data for aboveground biomass estimation, *Canadian Journal of Remote Sensing*, 36 (2): 129–141.

Duro, D.C., S.E. Franklin, and M.G. Dubé, 2013. Hybrid Object-based Change Detection and Hierarchical Image Segmentation for Thematic Map Updating, *Photogrammetric Engineering and Remote Sensing*, 79(3)259–268.

Duro, D.C., S.E Franklin, M.G. Dubé, 2012. A comparison of pixel-based and object-based image analysis with selected machine learning algorithms for the classification of agricultural landscapes using SPOT-5 HRG imagery, *Remote Sensing of Environment*, 118:259-272.

Elmore, A.J., J.F. Mustard, S.J. Manning, D.B. Lobell, 2000. Quantifying vegetation change in semiarid environments: precision and accuracy of spectral mixture analysis and the normalised difference vegetation index, *Remote Sensing of Environment*, 73:87–102.

Falkowski, M.J., P.E. Gessler, P. Morgan, A.T. Hudak, and, A.M.S. Smith, 2005. Evaluating ASTER satellite imagery and gradient modeling for mapping and characterizing wildland fire fuels. *Forest Ecology and Management*, 217:129–146.

Fiala, A.C.S., S.L. Garman, and A.N. Gray, 2006. Comparison of five canopy cover estimation techniques in the western Oregon Cascades. *Forest Ecology and Management*, 232:188–197.

Finney, M.A. 1998. FARSITE: fire area simulator-model development and evaluation. Rocky Mountain Research Station, US Department of Agriculture, Forest Service, Ogden, Utah. *Research Paper RMRS-RP* 4:47.

Gomez, C., J.C. White, and M.A. Wulder, 2011. Characterizing the state and processes of change in a dynamic forest environment using hierarchical spatio-temporal segmentation, *Remote Sensing of Environment*, 115:1665–1679

Goodwin N., N. C. Coops, C. Stone, 2005. Assessing plantation canopy condition from airborne imagery using spectral mixture analysis and fractional abundances, *International Journal of Applied Earth Observation and Geoinformation*, 7:11–28.

Goetz, S.J., A. Baccini, N.T. Laporte, T. Johns, W. Walker, and J. Kellndorfer, 2009. Mapping and monitoring carbon stocks with satellite observations: A comparison of methods. *Carbon Balance and Management*, 4:2. doi:10.1186/1750-0680-4-2.

Hall, F.G., K. Bergen, J.B. Blair, R. Dubayah, R. Houghton, and G. Hurtt, 2011. Characterizing 3D vegetation structure from space: Mission requirements, *Remote Sensing of Environment*, 115:2753–2775.

Hay G.J. and T. Blaschke, 2010. Forward: Special Issue on Geographic Object-Based Image Analysis (GEOBIA), *Photogrammetric Engineering and Remote Sensing*. 76(2)121-122.

Healey, S.P., W.B. Cohen, Y. Zhiqiang, and O. Krankina, 2005. Comparison of tasseled cap-based Landsat data structures for forest disturbance detection, *Remote Sensing of Environment*, 97(3):301-310. doi: 10.1016/j.rse.2005.05.009.

Hilker, T., M.A. Wulder, and N.C. Coops, 2008. Update of forest inventory data with lidar and high spatial resolution satellite imagery, *Canadian Journal of Remote Sensing*, 34:5−12.

Hopkinson, C., and L. Chasmer, 2009. Testing lidar models of fractional cover across multiple forest ecozones. *Remote Sensing of Environment*, 113:275–288.

Huang, C., B. Wylie, L. Yang, C. Homer, and G. Zylstra, 2002. Derivation of a tasselled cap transformation based on Landsat 7 at-satellite reflectance, *International Journal of Remote Sensing*, 23(8):1741−1748.

Hudak, A.T., M.A. Lefsky, W.B. Cohen, and M. Berterreche, 2002. Integration of LIDAR and Landsat ETM+ data for estimating and mapping forest canopy height, *Remote Sensing of Environment*, 82:397 − 416.

Hyde, P., R. Dubayah, B. Peterson, J.B. Blair, M. Hofton, C. Hunsaker, R. Knox, W. Walker, 2005. Mapping forest structure for wildlife habitat analysis using waveform lidar: Validation of montane ecosystems, *Remote Sensing of Environment*, 96:427 – 437.

Jennings, S.B., N.D. Brown, and D. Sheil, 1999. Assessing forest canopies and understory illumination: Canopy closure, canopy cover and other measures, *Forestry*, 72(1):59–73.

Koy, K., W.J. McShea, P. Leimgruber, B.N. Haack, and M. Aung, 2005. Percentage canopy cover — using Landsat imagery to delineate habitat for Myanmar's endangered Eld's deer (Cervus eldi), *Animal Conservation*, 8(3):289–296.

Lee, A.C., and R.M. Lucas, 2007. A lidar-derived canopy density model for tree stem and crown mapping in Australian forests. *Remote Sensing of Environment*, 111:493–518.

Lieffers, V.J., C. Messier, K.J. Stadt, F. Gendron, and P.G. Comeau, 1999. Predicting and managing light in the understory of boreal forests. *Canadian Journal of Forest Research*, 29:796–811.

Lobell, D.B., G.P. Asner, B.E. Law, and R.N. Treuhaft, 2002. View angle effects on canopy reflectance and spectral mixture analysis of coniferous forests using AVIRIS, *International Journal of Remote Sensing*, 23(11): 2247–2262.

Lovell, J.L., D.L.B. Jupp, D.S. Culvenor, and N.C. Coops, 2003. Using airborne and ground-based ranging lidar to measure canopy structure in Australian forests. *Canadian Journal of Remote Sensing*, 29:607–622.

Lu, D., M. Batistellas, E. Moran, and P. Mausel, 2004. Application of spectral mixture analysis to Amazonian land-use and land-cover classification. *International Journal of Remote Sensing*, 25(23):5345-5358.

Morgenstern k., A. Black, E. R. Humphreys, T.J. Griffis, B. Gordon, J.B. Drewitt, T. Cai, Z. Nesic, D.L. Spittlehouse, and N.J. Livingston, 2004. Sensitivity and uncertainty of the carbon

balance of a Pacific Northwest Douglas-fir forest during an El Nino/La Nina cycle, *Agricultural and Forest Meteorology*, 123:201–219.

Morsdorf, F., B. Kotz, E. Meier, K.I. Itten, and B. Allgower, 2006. Estimation of LAI and fractional cover from small footprint airborne laser scanning data based on gap fraction. *Remote Sensing of Environment*, 104:50–61.

Pascual, C., A. Garcia, W.B. Cohen, and S. Martin, 2010. Relationship between LiDAR-derived forest canopy height and Landsat image, *International Journal of Remote Sensing*, 31:1261–1280.

Peddle, D.R., F.G. Hall, E.F. LeDrew, 1999. Spectral mixture analysis and geometric-optical reflectance modelling of boreal forest biophysical structure, *Remote Sensing of Environment*, 67:288–297.

Powell, S.L., W.B. Cohen, S.P.Healey, R.E. Kennedy, G.G. Moisen, K.B. Pierce, and J.L. Ohmann, 2010. Quantification of live aboveground forest biomass dynamics with Landsat time-series and field inventory data: A comparison of empirical modeling approaches, *Remote Sensing of Environment*, 114(5):1053-1068. doi: 10.1016/j.rse. 2009.12.018.

Rollins, M.G., and C.K. Frame (editors), 2006. The LANDFIRE Prototype Project: Nationally Consistent and Locally Relevant Geospatial Data for Wildland Fire Management , USDA Forest Service, General Technical Report RMRS-GTR-175, Rocky Mountain Research Station, Fort Collins, Colorado, 416 p.

Smith, A.M.S., M. J. Falkowski, A. T. Hudak, J. S. Evans, A. P. Robinson, and C. M. Steele, 2009. A cross-comparison of field, spectral, and lidar estimates of forest canopy cover. *Canadian Journal of Remote Sensing*, 35:447–459.

Solberg, S., E. Næsset, K.H. Hanssen, and E. Christiansen, 2006. Mapping defoliation during a severe insect attack on Scots pine using airborne laser scanning. *Remote Sensing of Environment*, 102:364–376.

Somers, B., G.P. Asner, L. Tits, and P. Coppin, 2011. Endmember variability in Spectral Mixture Analysis: A review. *Remote Sensing of Environment*, 115:1603–1616.

Tompkins, S., J. F. Mustard, C. M. Pieters, and D. W. Forsyth, 1997. Optimization of endmembers for spectral mixture analysis. *Remote Sensing of Environment*, 59:472−489.

White, J.C., M.A. Wulder, C. Gomez, G. Stenhouse 2011. A history of habitat dynamics: Characterizing 35 years of stand replacing disturbance, *Canadian Journal of Remote Sensing*, 37(2):234-251.

Wulder, M.A., and S.E. Franklin, 2007. *Understanding Forest Disturbance and Spatial Pattern, Remote Sensing and GIS Approaches*, Taylor and Francis, Boca Raton, Florida, 28 p.

Wulder, M.A., S.E. Franklin, and J.C. White, 2004. Sensitivity of hyper clustering and labeling land cover classes to Landsat image acquisition date, *International Journal of Remote Sensing*, 10:5337−5344.

Wulder, M.A. and D. Seemann, 2003. Forest inventory height update through the integration of lidar data with segmented Landsat imagery, *Canadian Journal of Remote Sensing*, 29:536–543.

Wulder, M.A. J.C. White, M.M. Cranny, R.J. Hall, J.E. Luther, A.R. Beaudoin, D.G. Goodenough, and , J.A. Dechka, 2008. Monitoring Canada's forests. Part 1: Completion of the EOSD land cover project, *Canadian Journal of Remote Sensing*, 34(6):549-562.

Yu, Q., P. Gong, N. Clinton, B. Greg, M. Kelly, S. Dave, 2006. Object-based detailed vegetation classification with airborne high spatial resolution remote sensing imagery, *Photogrammetric Engineering and Remote Sensing*, 72:799–811.

Zeng, Y., M.E. Schaepman, B. Wu, J. Clevers, and A. Bregt, 2008. Scaling-based forest structural change detection using an inverted geometric-optical model in the Three Gorges region of China. *Remote Sensing of Environment*, 112:4261–4271.

Zhu Z., and C.E. Woodcock, 2011. Object-based cloud and cloud shadow detection in Landsat imagery, *Remote Sensing of Environment*, 118:83-94.

Table 1. LiDAR parameters.

Parameter	Performance
Sensor	Mark II
Laser scan frequency	25 Hz
Laser impulse frequency	40 000 Hz
Laser power	<4 W
Scan angle	±10°
Type of scanning mirror	Oscillating
Laser beam divergence	<0.5 mrad
Measurement decay	0.5-0.8 hits/m^2
Datum	NAD83
Projection	UTM Zone 10
Platform	Bell 206 Jet Ranger helicopter
Flight altitude above ground	900m
Flight speed	25-30 m/s
Version of TerraScan used to classify	Version 004.006

Table 2. Correlation coefficients between LiDAR canopy cover and Landsat-derived TCA and endmember fractions.

	TCA	Sunlit canopy	NPV	Shade	Exposed soil	Canopy cover
TCA	1.0	0.66	0.31	0.02	0.46	0.86
Sunlit canopy	0.66	1.0	-0.90	-0.94	0.04	0.68
NPV	0.31	-0.90	1.0	0.81	-0.27	-0.22
Shade	0.02	-0.94	0.81	1.0	-0.24	-0.34
Exposed soil	0.46	0.04	-0.27	-0.24	1.0	-0.20
Canopy cover	0.86	0.68	-0.22	-0.34	-0.20	1.0

Table 3. Coniferous regression models obtained with R^2 of ≥ 0.65 (n=40 per equation).

Regression equation	R^2	SE	RMSE
$CC = -0.194 + 0.273sun - 0.34soil + 0.25TCA$	0.78	0.15	0.39
$CC = 0.308 - 0.31sun - 0.38\ soil$	0.71	0.21	0.46
$CC = 0.768 + 0.27NPV - 0.35soil + 1.81TCA$	0.65	0.47	0.69
$CC = 0.354 - 0.31shade - 0.43soil + 0.004TCA$	0.65	0.50	0.71

Table 4. Deciduous regression models obtained with R^2 of ≥ 0.65 (n=60 per equation)

Regression equation	R^2	SE	RMSE
$CC = 0.261 + 0.185sun - 0.237soil + 0.328TCA$	0.81	0.11	0.34
$CC = 0.439 - 0.212sun - 0.258\,soil$	0.73	0.16	0.40
$CC = 0.421 + 0.393NPV - 0.471soil + 0.495TCA$	0.69	0.23	0.48

Table 5. Percent homogeneous cover for landscape elements of variable size.

Mean Object Size	% Homogeneous Cover
1 ha	82.1
1.5 ha	84.2
2 ha	85.2
2.5 ha	86.6
3 ha	87.5
3.5 ha	87.8

Table 6. Coniferous regression models obtained with R^2 of ≥ 0.60 (n=40 per equation).

Regression equation	MOS	R^2	SE	RMSE
$CC = -0.225 + 0.15sun - 0.28soil + 0.195TCA$	2.5	0.82	0.17	0.42
$CC = 0.411 - 0.25sun - 0.39\ soil$	3.0	0.75	0.31	0.56
$CC = 0.273 - 0.21shade - 0.34soil + 0.45TCA$	2.0	0.62	0.47	0.69

Table 7. Deciduous regression models obtained with R^2 of ≥ 0.60 (n=40 per equation).

Regression equation	MOS	R^2	SE	RMSE
$CC = 0.171 + 0.285sun - 0.11soil + 0.328TCA$	2.5	0.86	0.07	0.28
$CC = 0.224 - 0.153shade - 0.281soil + 0.31TCA$	3.0	0.77	0.16	0.41
$CC = 0.19 - 0.277sun - 0.295\ soil$	2.0	0.61	0.54	0.74

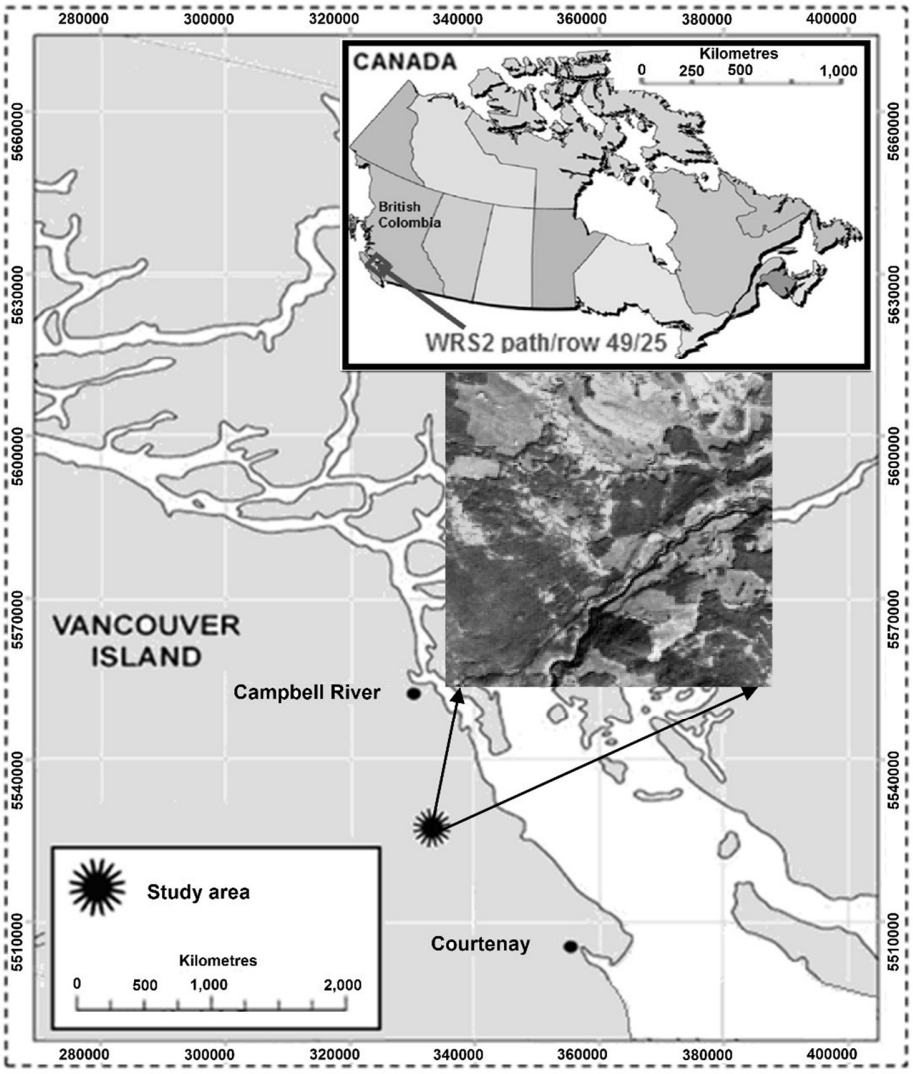

Fig. 1. Study area located between Courtenay and Campbell River, Vancouver Island, British Columbia, Canada.

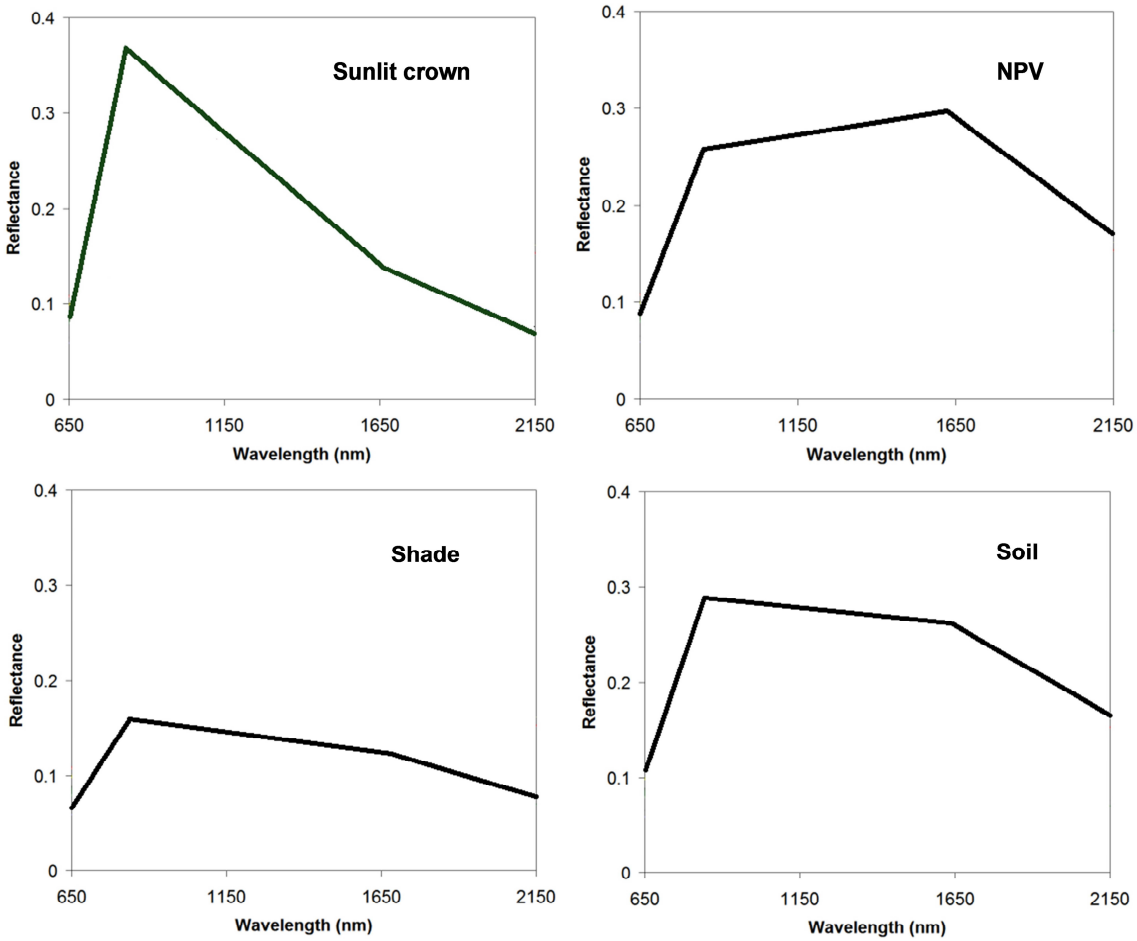

Fig. 2. Endmember spectral characteristics derived from Landsat shortwave-infrared, near-infrared and red bands.

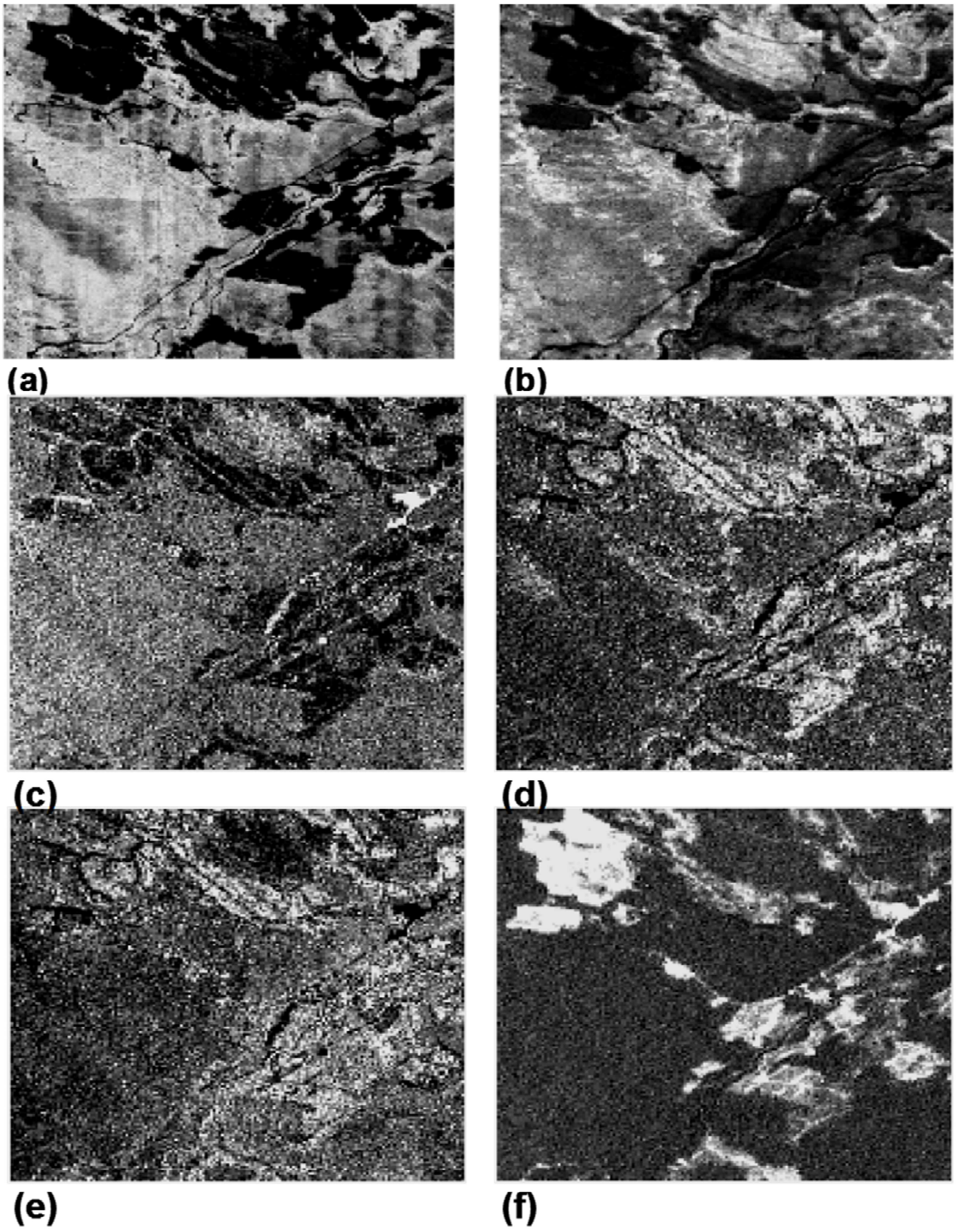

Fig. 3. (a) LiDAR derived canopy cover. (b) Tasseled Cap Angle (TCA). (c) Sunlit crown, (d) NPV, (e) shade and (f) exposed soil.